



OPEN ACCESS

EDITED BY

Kyung-Ae Park,
Seoul National University,
Republic of Korea

REVIEWED BY

Joseph Kojo Ansong,
University of Ghana, Ghana
YoungHo Kim,
Pukyong National University,
Republic of Korea

*CORRESPONDENCE

Ru Chen

✉ ruchen@alum.mit.edu

RECEIVED 02 February 2023

ACCEPTED 07 June 2023

PUBLISHED 30 June 2023

CITATION

Zhang G, Chen R, Li L, Wei H and Sun S
(2023) Global trends in surface eddy mixing
from satellite altimetry.
Front. Mar. Sci. 10:1157049.
doi: 10.3389/fmars.2023.1157049

COPYRIGHT

© 2023 Zhang, Chen, Li, Wei and Sun. This is an open-access article distributed under the terms of the [Creative Commons Attribution License \(CC BY\)](https://creativecommons.org/licenses/by/4.0/). The use, distribution or reproduction in other forums is permitted, provided the original author(s) and the copyright owner(s) are credited and that the original publication in this journal is cited, in accordance with accepted academic practice. No use, distribution or reproduction is permitted which does not comply with these terms.

Global trends in surface eddy mixing from satellite altimetry

Guangchuang Zhang¹, Ru Chen^{1*}, Laifang Li^{2,3,4}, Hao Wei¹ and Shantong Sun⁵

¹School of Marine Science and Technology, Tianjin University, Tianjin, China, ²Department of Meteorology and Atmospheric Science, The Pennsylvania State University, University Park, PA, United States, ³Institute of Computational and Data Science, The Pennsylvania State University, University Park, PA, United States, ⁴Earth and Environmental System Institute, The Pennsylvania State University, University Park, PA, United States, ⁵Department of Earth, Ocean & Atmospheric Science, Florida State University, Tallahassee, FL, United States

Mixing induced by oceanic mesoscale eddies can affect tracer distributions in the ocean and thus modulate the evolution of the physical and biochemical marine system. In the context of global warming, regionally different trends in eddy mixing could exist. Motivated by this hypothesis, we quantified the trend in surface eddy diffusivity, a metric widely used to quantify the eddy mixing rate, in the global ocean using satellite altimetry data. The global average of the particle-based eddy diffusivity increases by $284.1 \text{ m}^2\text{s}^{-1}$ per decade during the period of 1994–2017, or 3.7% per decade relative to its climatological mean value. In 54% of the global ocean, eddy diffusivity shows an increasing trend. The diffusivity trend can be decomposed into two components: one related to changes in eddy mixing length and the other related to eddy velocity magnitude. In 73% of the global ocean, changes in eddy mixing length account for more than 50% of the diffusivity trend. The suppressed mixing length theory (SMLT) is employed to interpret the trend in eddy mixing length. SMLT well captures the sign of the trend in two of the representative regions. Among all the parameters (e.g., eddy size, phase speed) inherent in SMLT, the eddy velocity magnitude plays a dominant role in determining the trend in the SMLT-based eddy mixing length. Diagnosing the geostrophic eddy kinetic energy budget reveals that the dominant mechanism for the trend in eddy velocity magnitude is the pressure work induced by ageostrophic flows. Our results suggest that a time-dependent eddy parameterization scheme should be employed in non-eddy-resolving models to account for the trend in eddy mixing.

KEYWORDS

oceanic mesoscale eddies, trend, eddy diffusivity, eddy mixing length, eddy velocity magnitude

1 Introduction

Mesoscale eddies, ubiquitous in the global ocean, contain about 90% of the ocean's kinetic energy (Ferrari and Wunsch, 2009). Eddy mixing influences the distribution of heat, salinity, and nutrients, and thus play an important role in modulating the variability of the climate system and marine ecosystem (Stammer, 1998; Gnanadesikan et al., 2015). The effect of eddy mixing is often parameterized in non-eddy-resolving climate models. Reasonable choice of eddy parameterization schemes is crucial for the realism of model simulation (Fox-Kemper et al., 2019). When implementing eddy parameterization schemes, a steady eddy diffusivity coefficient is often used (Gent and McWilliams, 1990; Griffies, 1998; Abernathy et al., 2011; Sun et al., 2021). However, in the context of global warming, significant trends have been found in ocean temperature and salinity, sea level, upper-ocean stratification, eddy kinetic energy (EKE) and ocean circulation (Church et al., 2011; Du et al., 2015; Hogg et al., 2015; Nan et al., 2015; Steinkamp and Gruber, 2015; Beal and Elipot, 2016; Landschützer et al., 2016; Patara et al., 2016; Syst et al., 2018; Yamaguchi and Suga, 2019; Johnson and Lyman, 2020; Martínez-Moreno et al., 2021; Beech et al., 2022; Lee et al., 2022; Peng et al., 2022; Risaro et al., 2022). It remains unclear whether a trend in oceanic mesoscale eddy mixing exists in the context of this climate change. Failure to consider this potential trend in eddy diffusivity may increase the uncertainty of climate simulations. Because climate model results are sensitive to the choice of eddy diffusivity (Danabasoglu and Marshall, 2007; Gnanadesikan et al., 2015). Therefore, this study aims to estimate and interpret the long-term trend of global surface cross-stream eddy diffusivities, which represent eddy mixing rate in the cross-mean flow direction.

Previous studies have shown that eddy diffusivity has significant spatiotemporal variability (e.g., Abernathy and Marshall, 2013; Chen et al., 2014b; Griesel et al., 2014; Busecke et al., 2017; Bolton et al., 2019; Guan et al., 2022). For example, Busecke and Abernathy (2019) found eddy mixing is linked with large-scale climate variability (e.g., El Niño-Southern Oscillation). However, few studies have provided quantitative estimates of the long-term changes in global surface cross-stream diffusivity. On the other hand, much evidence exists about the long-term trend in EKE and ocean circulation (Hogg et al., 2015; Beal and Elipot, 2016; Patara et al., 2016; Hu et al., 2020; Martínez-Moreno et al., 2021; Beech et al., 2022; Peng et al., 2022). Based on the mixing length theory and the suppressed mixing length theory (SMLT), both EKE and ocean circulation influence eddy diffusivity. Therefore, we propose that eddy diffusivity also has a significant trend in the global ocean. Specifically, the mixing length theory indicates that the eddy diffusivity is proportional to the product of eddy mixing length and eddy velocity magnitude (Taylor, 1915). Based on SMLT from Ferrari and Nikurashin (2010), cross-stream eddy mixing length is linked with eddy and mean flow properties (e.g., eddy size, phase speed, and eddy velocity magnitude).

To verify our hypothesis that eddy diffusivity has a significant trend in the global ocean, we need to estimate the global trend in surface eddy mixing. Specifically, using the Lagrangian particle

approach, we first estimate the cross-stream eddy diffusivities in each year from the altimeter data. Then we estimate the trend in eddy diffusivity using the Theil-Sen estimator method (Theil, 1950; Sen, 1968). The Lagrangian particle method has been demonstrated to be effective in providing realistic and converged eddy diffusivity (e.g., Lumpkin and Elipot, 2010; Rypina et al., 2012; Chen et al., 2014b; Chen et al., 2017; Guan et al., 2022). We chose to use altimeter data because it has been proven effective in capturing the trends in ocean state (e.g., Lee et al., 2022; Peng et al., 2022).

Besides estimating mixing trends, we also aim to discuss the underlying mechanism of the trend in eddy mixing. This effort may shed light on the development of the long-term mixing trend parameterization. Using a trend decomposition method from Guo et al. (2022), we decompose the diffusivity trend into two components: One related to eddy velocity magnitude, and the other related to eddy mixing length. This decomposition can help quantify the respective contribution of eddy velocity magnitude and eddy mixing length to the diffusivity trend. We then discuss the mechanism modulating the trends in eddy velocity magnitude and eddy mixing length. For the former, we employ a novel budget of geostrophic kinetic energy. For the latter, we test the validity of SMLT in representing the trend of cross-stream eddy mixing lengths (Ferrari and Nikurashin, 2010). SMLT is capable of capturing the sign of eddy mixing trend in only two of the total five regions we consider. The origin of the trend in SMLT-based eddy mixing length is also discussed through trend decomposition.

To summarize, we aim to estimate the trend in global surface eddy diffusivity and explore the underlying mechanisms. This paper is organized as follows. Section 2 describes the dataset and presents the method for mixing and trend estimation. In section 3, we describe the trends in global surface cross-stream eddy diffusivity from both the global and regional perspectives. The respective contribution of eddy mixing length and eddy velocity magnitude to the mixing trend is quantified. Sections 4 and 5 aim to interpret the trend in eddy mixing length using SMLT. Section 4 introduces the decomposition method of the SMLT-based eddy mixing lengths, whose corresponding result is presented in section 5. Section 6 discusses the underlying mechanism of the trend in eddy velocity magnitude. Section 7 is a summary.

2 Data and method

2.1 Data

2.1.1 AVISO data and numerical particles

For diffusivity estimation, we use the geostrophic velocity data from the Archival Verification and Interpretation of Satellite Oceanographic Data (AVISO, <http://www.aviso.altimetry.fr/>) of the French National Space Agency. The daily velocity fields we use have a spatial resolution of 0.25° and span the time period 1994–2017. This dataset has been successfully applied in previous studies about eddy diffusivity and eddy/mean flow parameters (e.g., Abernathy and Marshall, 2013; Hogg et al., 2015; Bolton et al., 2019; Martínez-Moreno et al., 2021).

Following a series of previous work, we use the Lagrangian particle approach to estimate the Lagrangian eddy diffusivity in each year (Sallee et al., 2011; Chen and Waterman, 2017; Guan et al., 2022). An offline advection approach is used to obtain the particle trajectories covering the entire globe during 1994–2017. Taking the year 1996 as an example, we deployed virtual numerical particles offline in the global region with a resolution of 0.2°. These particles were advected by the AVISO geostrophic velocity field during 1996 based on the fourth-order Runge-Kutta method. The daily particle position and velocity information is recorded. Particles that were deployed at or advected to the land points were set to be NaN. As an example, Figure 1A shows sample particle trajectories, which were randomly selected, in the global ocean during 1996. Only 0.23% of the total number of particle trajectories are shown to make these tracks visible.

2.1.2 OSCAR data

Based on the mixing length theory, the diffusivity trend inferred from the AVISO geostrophic velocity field is linked with the trend of geostrophic eddy velocity magnitude u_{rms} (Taylor, 1915). Here

$$u_{rms} = \sqrt{u_g'^2 + v_g'^2} = \sqrt{2EKE}, \tag{1}$$

where $'$ is the deviation of the daily geostrophic velocity from the annual mean, and the subscript g represents the geostrophic flow. To interpret the trend of u_{rms} , we diagnose the geostrophic EKE budget for each year (for details of the budget equation, see Supplementary Material 2). Considering that the ocean system is nonlinear, and geostrophic motions are coupled with ageostrophic

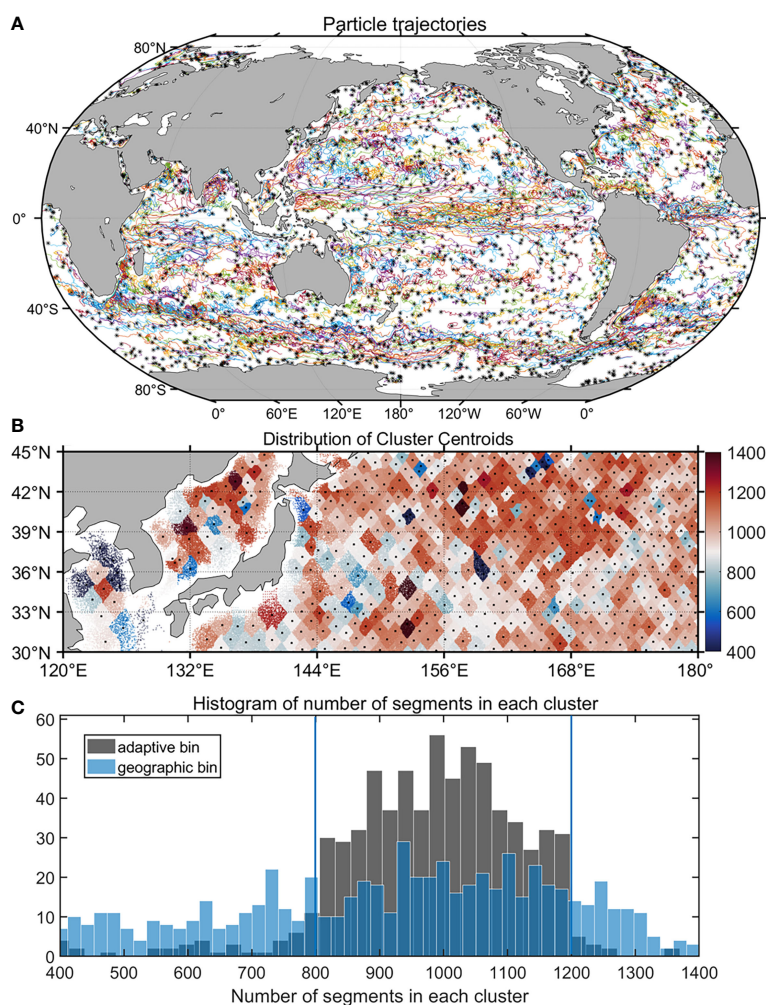


FIGURE 1
(A) Sample particle trajectories released on the first day of 1996. Only 0.23% of particle trajectories are randomly selected here to make these tracks visible. **(B)** The distribution of the centroid for each adaptive bin (black dots) in the region located at 30°N–45°N 120°E–180° of 1996. The color indicates the number of pseudo-trajectories in each adaptive bin. **(C)** Histogram of the number of pseudo-trajectories within each adaptive bin in panel B (gray bars) and that in each 1°×1° geographic bin (blue bars). The blue lines indicate the numbers 800 and 1200.

ones, the information about both geostrophic and ageostrophic velocities is needed to diagnose the geostrophic EKE budget.

To obtain the ageostrophic velocity field, we chose to use the widely used surface velocity product: the Ocean Surface Current Analyses Real-time dataset (OSCAR). For details of OSCAR, see [Bonjean and Lagerloef \(2002\)](#) and [Dohan \(2017\)](#). The area covered by OSCAR has expanded from the equatorial region (Lagerloef et al., 1999) to the entire globe, providing daily surface currents velocity on a global 0.25° × 0.25° grid. Consistent with AVISO, we chooseto use the OSCAR data during the period 1994-2017.

The surface total velocity from OSCAR is calculated from a simplified physical model,

$$fk \times U_o = -\frac{1}{\rho} \nabla p + \frac{1}{\rho} \frac{\partial \tau}{\partial z}, \quad (2)$$

where f is Coriolis parameter, $U_o = u_o i + v_o j$, representing total velocity from OSCAR, ρ is the sea surface density, p is the sea surface pressure, and τ is the surface wind stress. Satellite-observed datasets including sea surface height gradients, ocean vector winds and sea surface temperature gradients were used to produce the OSCAR dataset. Equation (2) shows that this model contains geostrophic, Ekman, and thermal wind dynamics.

Subtracting the AVISO geostrophic velocity from OSCAR total velocity (U_o) leads to the ageostrophic velocity. The physical model [Equation (2)] indicates that the ageostrophic flow inferred from OSCAR mainly contains the Ekman flow. Considering that this model is linear and does not capture nonlinear dynamics, other components (e.g., submesoscale ageostrophic motions) are not well captured by OSCAR. Nonetheless, much evidence has demonstrated that this dataset is useful for studies about mesoscale eddies and the EKE budget. For example, using OSCAR data, [Chen et al. \(2018\)](#) studied the spatial distribution and seasonal variability of EKE in the Bay of Bengal region. [Piontkovski et al. \(2019\)](#) investigated the interannual variability of the occurrence of mesoscale eddies in the western Arabian Sea. In addition, although surface drifter data may provide more realistic total velocity fields, its non-uniform spatiotemporal distribution make it challenging to diagnose the EKE budget at drifter points ([Yu](#)

[et al., 2019](#)). Therefore, we use the OSCAR dataset to infer the ageostrophic velocity.

2.2 Method

2.2.1 Mixing estimation method

Following a series of previous studies (e.g., [Chen et al., 2014b](#); [Chen et al., 2017](#); [Guan et al., 2022](#)), we estimate the cross-stream eddy diffusivity using a Lagrangian autocorrelation function based on particle trajectories. This approach is generally termed as the Lagrangian particle method and have been proven effective for converged diffusivity estimates ([Davis, 1987](#); [Davis, 1991](#); [LaCasce and Bower, 2000](#); [Zhurbas and Oh, 2004](#); [Lumpkin and Elipot, 2010](#); [Rypina et al., 2012](#); [Chen et al., 2014b](#); [Chen et al., 2017](#); [Guan et al., 2022](#)). The diagnostic formula for cross-stream (i.e., cross-mean flow) eddy diffusivity is

$$\kappa_{\perp,particle}(\mathbf{x}) = \lim_{\tau \rightarrow \infty} \kappa_{\perp}(\mathbf{x}, \tau) \approx \frac{\int_{\tau_1}^{\tau_2} \kappa_{\perp}(\mathbf{x}, \tilde{\tau}) d\tilde{\tau}}{\tau_2 - \tau_1}, \quad (3)$$

where

$$\kappa_{\perp}(\mathbf{x}, \tau) = \int_0^{\tau} d\tilde{\tau} \langle u'_{g\perp}(t_0 | \mathbf{x}, t_0) u'_{g\perp}(t_0 + \tilde{\tau} | \mathbf{x}, t_0) \rangle_L. \quad (4)$$

Here the bracket $\langle \cdot \rangle$ represents the ensemble average of all the pseudo-trajectories passing the adaptive bin centered at \mathbf{x} . For example, [Figure 2A](#) shows sample pseudo-trajectories through the adaptive bin centered at (167.91°E, 53.41°N). $u'_{g\perp}(t_0 + \tilde{\tau} | \mathbf{x}, t_0)$ represents the cross-stream geostrophic eddy velocity at time $t_0 + \tilde{\tau}$ at the position of the particle, which passes the position \mathbf{x} at time t_0 . As τ increases, the velocity gradually gets decorrelated with the initial velocity and $\kappa_{\perp}(\mathbf{x}, \tau)$ asymptotes to a constant value, i.e., has converged. The Lagrangian equilibration time τ_{eq} is the minimum time it takes for $\kappa_{\perp}(\mathbf{x}, \tau)$ to level off. We use the criteria from [Chen and Waterman \(2017\)](#) to judge whether $\kappa_{\perp}(\mathbf{x}, \tau)$ has leveled off. In brief, when the change rate of the fitted $\kappa_{\perp}(\mathbf{x})$ over a 30-day period (i.e. $[\tau_1, \tau_2]$) is less than the minimum value of two standard

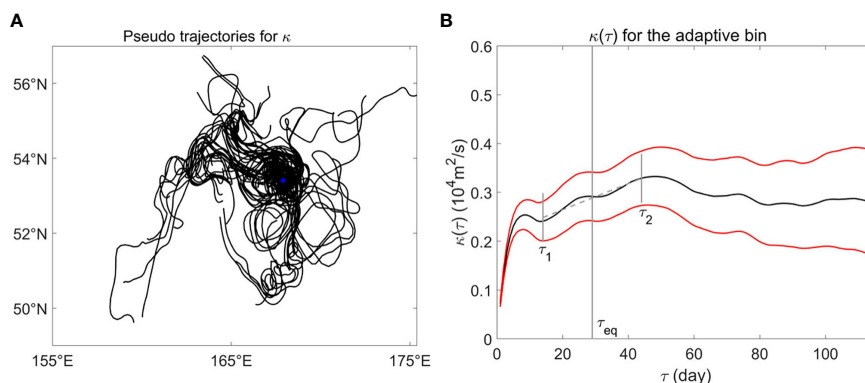


FIGURE 2

(A) Sample pseudo-trajectories through the adaptive bin centered at 167.91°E, 53.41°N. The blue dot shows the centroid of the adaptive bin. (B) $\kappa_{\perp}(\mathbf{x}, \tau)$ [Equation 4] as a function of τ in the adaptive bin from (A). Red lines show the uncertainties of $\kappa_{\perp}(\mathbf{x}, \tau)$ at the 95% confidence level via a bootstrapping method. The vertical grey line indicates the equilibration time τ_{eq} , where $\kappa_{\perp}(\mathbf{x}, \tau)$ starts leveling off.

errors during that period, we consider $\kappa_{\perp}(x)$ has leveled off. Here $\tau_{eq} = (\tau_{1s} + \tau_{2s})/2.0$, where $[\tau_{1s}, \tau_{2s}]$ denotes the smallest $[\tau_1, \tau_2]$ with converged $\kappa_{\perp}(x, \tau)$. As an example, the grey line in Figure 2B shows τ_{eq} in the adaptive bin centered at (167.91°E, 53.41°N).

We chose to use pseudoparticle trajectories instead of the original particle trajectories to improve the convergence of eddy diffusivity (Chen et al., 2014b; Chen et al., 2017; Guan et al., 2022). Specifically, a point is selected every few days from the original trajectory as the initial position of the pseudo-trajectory, and a certain track length for the pseudo-trajectory is selected. It can increase the number of trajectories and make diffusivity converge (Griesel et al., 2010; Klocker et al., 2012). To ensure the convergence of eddy diffusivity, the length of pseudo-trajectories should be longer than the Lagrangian equilibrium time. Yet, the longer the pseudo-trajectory is, the smaller the number of pseudo trajectories is. And adequate amount of pseudo trajectories in each bin is a prerequisite for obtaining converged diffusivity estimates. Considering this, we choose 115 days to be the pseudo-trajectory length in this study. The interval between the adjacent initial positions of pseudo-trajectories is chosen to be five days.

To further improve the convergence of eddy diffusivity, we choose to use the adaptive-bin method based on the K-means algorithm (Koszalka and LaCasce, 2010; Chen et al., 2014b; Guan et al., 2022) instead of the geographic bin method. Due to the flow inhomogeneity, the number of pseudo-trajectories in the regular geographic bins varies greatly (Figure S1 in Supplementary Material), leading to poor convergence of diffusivity estimates. As an example, the blue bars in Figure 1C show the histogram of the number of pseudo-trajectories in each 1°×1° geographic bin in a selected region located at 30°N-45°N 120°E-180°. The histogram has a wide shape and the number of tracks ranges from 400-1400. The advantage of using adaptive bins instead of geographic bins is that the K-means algorithm can make sure the number of the tracks in each bin is roughly the same. Take the region located at 30°N-45°N 120°E-180° as an example, the adaptive bins are randomly distributed in this area (Figures 1B, C). However, the number of pseudo-trajectories in each adaptive bin is roughly uniform ranging from 800 to 1200. In this case, the average size of adaptive bins in the global ocean is roughly 1°×1°. We find that increasing the number of pseudo-trajectories in each adaptive bin will increase the size of adaptive bins and thus decrease the spatial resolution of our eddy mixing estimates. However, the large-scale structures of eddy diffusivities is insensitive to this change.

2.2.2 Trend estimation method

We chose to use the Theil-Sen estimator (TS) approach (Theil, 1950; Sen, 1968) for trend estimation in this study. The TS method is a robust non-parametric statistical method for estimating trends. The disadvantage of the commonly used simple linear regression method is that the estimated trend is sensitive to the outliers in time series (Ohlson and Kim, 2015). In contrast, the TS method is insensitive to both the outliers and uncertainties in time series. Therefore, the TS method has been widely used in the analysis of trend in meteorological and oceanographic variables (Gocic and Trajkovic, 2013; Sa'adi et al., 2019; Zhao et al., 2022).

The statistical significance of the estimated trend is assessed through a modified Mann-Kendall test (Mann, 1945; Kendall, 1948; Hamed and Rao, 1998). This method has been widely used to determine the statistical significance of the estimated trend (Yue and Wang, 2004; Hu et al., 2020; Zhao et al., 2022). The advantage of this method is that it neither requires the time series to be in a normal distribution nor requires the trend to be linear. In addition, it is neither affected by missing values nor influenced by abnormal data points. Furthermore, this method can effectively eliminate the impact of serial correlation on the estimated trend. Thus, it can be used to assess the trend significance for the time series with autocorrelation (Hamed and Rao, 1998).

3 Trends in eddy mixing

3.1 Global analysis

3.1.1 Spatial structure

The trend of $\kappa_{\perp,particle}$ in the global ocean has large spatial variability (Figure 3A). The trend magnitude is large in the western boundary currents and their extension regions, the equatorial Indian Ocean, and the central equatorial Pacific Ocean. In particular, there is a significant increase trend of $\kappa_{\perp,particle}$ in the equatorial Pacific Ocean, with a magnitude as large as 5000 m²s⁻¹ per decade. In the western boundary currents and their extension regions, the structure of the $\kappa_{\perp,particle}$ trend is patchy. The trend is negative in the upstream of the Kuroshio Extension, but positive in the downstream. The opposite occurs at the Gulf Stream Extension, with positive (negative) trend in the upstream (downstream).

From a global perspective, the trend of the globally integrated $\kappa_{\perp,particle}$, inferred from the TS method, is 284.1 m²s⁻¹ per decade (Figure 4). It accounts for 3.7% of the climate-mean $\kappa_{\perp,particle}$. $\kappa_{\perp,particle}$ shows an increasing trend in 54% of the global ocean. Among these areas with an increasing trend, 17.7% is significant at the 95% confidence level.

Based on the mixing length theory (Taylor, 1915), eddy diffusivity is proportional to the product of eddy mixing length and eddy velocity magnitude. Therefore, the particle-based eddy mixing length,

$L_{mix,particle}$, can be diagnosed from

$$L_{mix,particle} = \frac{\kappa_{\perp,particle}}{\Gamma u_{rms}}. \quad (5)$$

Here u_{rms} is eddy velocity magnitude and Γ is the mixing efficiency with magnitude of O(1). Following previous studies, we choose Γ to be 0.35 (e.g., Chen et al., 2014b; Chen et al., 2017; Busecke and Abernathy, 2019; Guan et al., 2022). Equation (5) indicates that both the trend in $L_{mix,particle}$ and the trend in u_{rms} contribute to the trend in $\kappa_{\perp,particle}$. Positive trends in $L_{mix,particle}$ and u_{rms} lead to increasing trend in $\kappa_{\perp,particle}$. On the other hand, negative trends of these two factors lead to decreasing trend in $\kappa_{\perp,particle}$.

Since the trend of $\kappa_{\perp,particle}$ arises from the trends in $L_{mix,particle}$ and u_{rms} . Here we assess the global trend distributions of both $L_{mix,particle}$ and u_{rms} (Figures 3B, C). Compared to the trend in u_{rms} ,

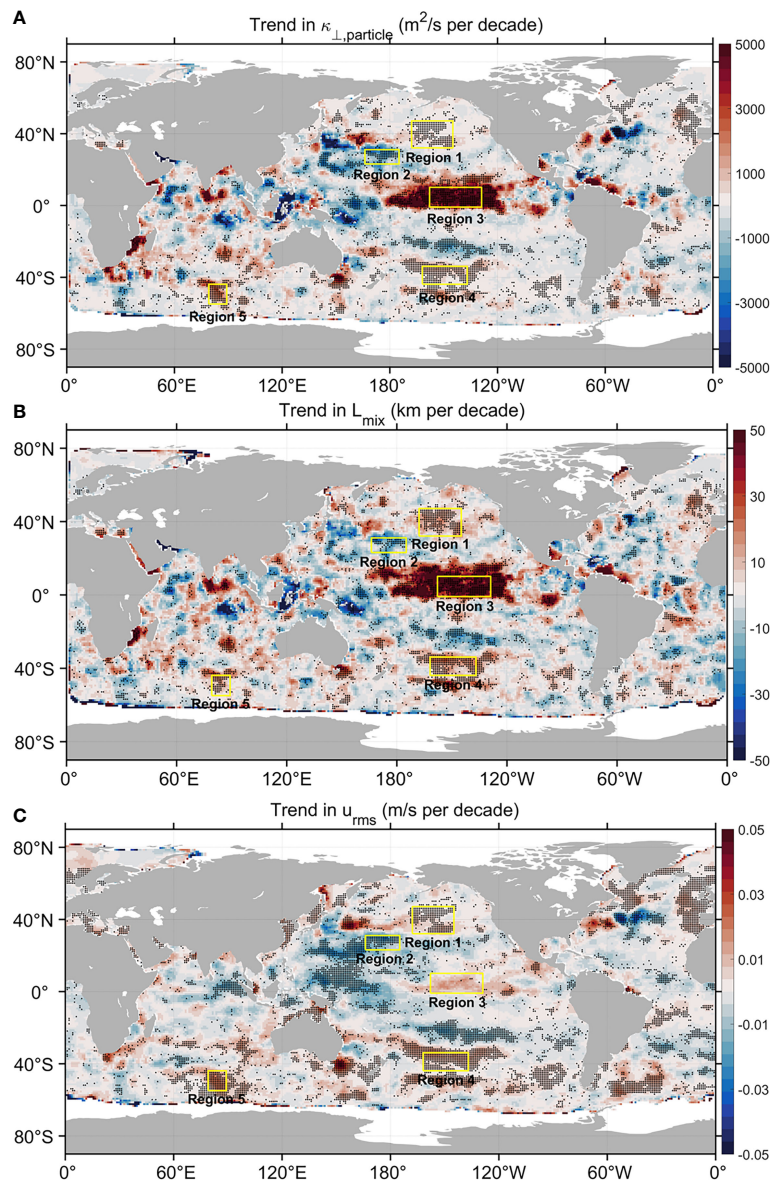


FIGURE 3

The trend of (A) $\kappa_{L,particle}$, (B) $L_{mix,particle}$, and (C) u_{rms} in the global ocean during the period 1994–2017. The trend diagnosis method is described in section 2.2.2. Black dots indicate the grid points, where the trend is statistically significant at the 95% confidence level. Yellow boxes show the five representative regions we discuss.

the global structure of the $L_{mix,particle}$ trend resembles more to that of the $\kappa_{L,particle}$ trend. Similar to $\kappa_{L,particle}$, the large magnitude of the $L_{mix,particle}$ trend occurs in the western boundary currents and their extension regions, the equatorial Indian Ocean, and the central equatorial Pacific Ocean. In contrast, the large trend in u_{rms} only occurs in the western boundary currents and their extension regions. In the central equatorial Pacific Ocean, the trend of $L_{mix,particle}$ increases significantly, with a magnitude as large as 50 km per decade. In contrast, the increasing trend of u_{rms} is insignificant in the central equatorial Pacific Ocean.

Our analysis in Figure 5 indicates that compared to u_{rms} , the trend of $L_{mix,particle}$ contributes more to that of $\kappa_{L,particle}$. The correlation coefficient of the trends between $L_{mix,particle}$ and $\kappa_{L,particle}$ reaches 0.69. The errorbar, based on a bootstrapping

technique (Chernick, 2011; Chen et al., 2014b; Schulte et al., 2016; Ivanova et al., 2021), is 0.02 at the 95% confidence level (Figure 5A). Concerning u_{rms} , its trend is also positively correlated with the $\kappa_{L,particle}$ trend, with a weaker correlation magnitude though (0.37 ± 0.02 at the 95% confidence level) (Figure 5A). In 89% (75%) of the global ocean area the sign of the trend in $L_{mix,particle}(u_{rms})$ is consistent with that of $\kappa_{L,particle}$ (Figure 5B).

3.1.2 Decomposition of the mixing trend

Although the mixing length theory [Equation (5)] suggests that eddy diffusivity is proportional to eddy velocity magnitude and eddy mixing length, it remains unclear which of these two factors contributes more to the diffusivity trend. To quantify the contribution of each factor to the trend in eddy diffusivity, we

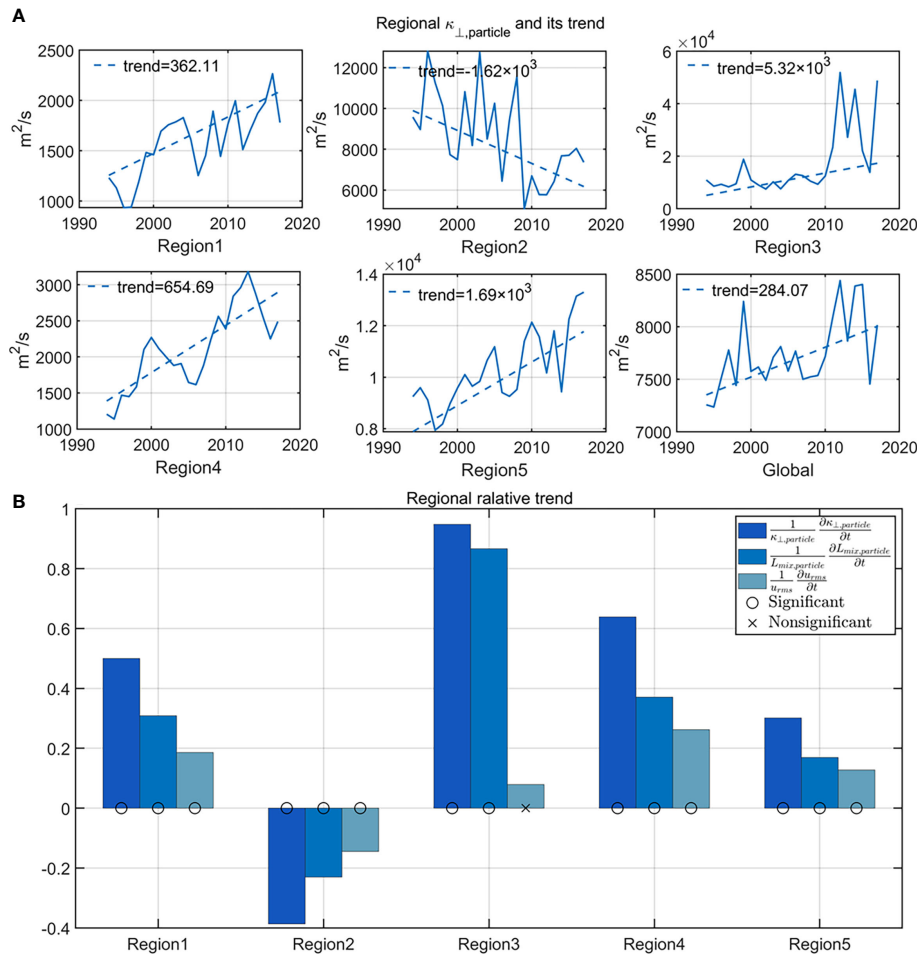


FIGURE 4 (A) The spatially averaged $\kappa_{\perp,particle}$ time series (blue solid line) and its trend (blue dashed line, m^2s^{-1} per decade) in both the five representative regions and the global ocean. These representative regions are indicated in Figure 3. (B) The relative trends of $\kappa_{\perp,particle}$, $L_{mix,particle}$, and u_{rms} [Equation (6)] in the five representative regions during 1994-2017. Statistically insignificant trends at the 95% confidence level are marked by "x", and significant trends are marked by "o".

introduce a metric “relative trend”. Then we employ a trend decomposition method to quantitatively decompose the relative trend of $\kappa_{\perp,particle}$ into two components: One related to $L_{mix,particle}$ and the other related to u_{rms} [Equation (6)]. This decomposition approach is inspired by Guo et al. (2022), who successfully decomposed the trend in eddy heat flux into components related to the velocity variance, temperature variance, and coherence parameters, respectively. By taking the logarithm on both sides of Equation (5) and then computing their temporal derivatives, the relative trend of $\kappa_{\perp,particle}$ can be expressed as

$$\frac{1}{\kappa_{\perp,particle}} \frac{\partial \kappa_{\perp,particle}}{\partial t} = \frac{1}{u_{rms}} \frac{\partial u_{rms}}{\partial t} + \frac{1}{L_{mix,particle}} \frac{\partial L_{mix,particle}}{\partial t}. \quad (6)$$

That is, the relative trend of $\kappa_{\perp,particle}$ is equal to the sum of the relative trend in $L_{mix,particle}$ and that in u_{rms} . Using Equation (6), one can quantify the contribution of each factor to the relative trend of $\kappa_{\perp,particle}$.

We estimated the relative trends in $\kappa_{\perp,particle}$, $L_{mix,particle}$ and u_{rms} in the global ocean (Figure 6). The relative trend of $\kappa_{\perp,particle}$ has elevated positive values in the equatorial central Pacific and at high latitudes of the northeast Pacific and Atlantic Oceans. Its value is

also significantly large around 40°S in the central Pacific. However, the relative trend in $\kappa_{\perp,particle}$ is negative at 20°S-30°N in the western Pacific. Similar to $\kappa_{\perp,particle}$, the relative trend in $L_{mix,particle}$ also has significant positive values in the central equatorial Pacific and at the high-latitude Pacific. Concerning the relative trend in u_{rms} , it is generally positive in the Southern Ocean and at high-latitude regions of the Northern Hemisphere. In the equatorial eastern Pacific, the relative trend of u_{rms} is positive but smaller than that at high-latitudes. In contrast, the relative trend of u_{rms} is negative in both the equatorial western Pacific and the mid-latitude Pacific.

To assess the respective contribution of $L_{mix,particle}$ and u_{rms} to the relative trend in $\kappa_{\perp,particle}$, we diagnosed the ratio of the relative trends between $L_{mix,particle}$ and $\kappa_{\perp,particle}$ and that between u_{rms} and $\kappa_{\perp,particle}$. A positive (negative) ratio of the relative trends between $L_{mix,particle}$ and $\kappa_{\perp,particle}$ indicates that $L_{mix,particle}$ has a positive (negative) effect on the relative trend of $\kappa_{\perp,particle}$. We can also interpret the contribution of u_{rms} to $\kappa_{\perp,particle}$ in an analogous way. Our results, shown in Figures 7A and 6B, suggest that compared to u_{rms} , $L_{mix,particle}$ contributes much more to the relative trend in $\kappa_{\perp,particle}$.

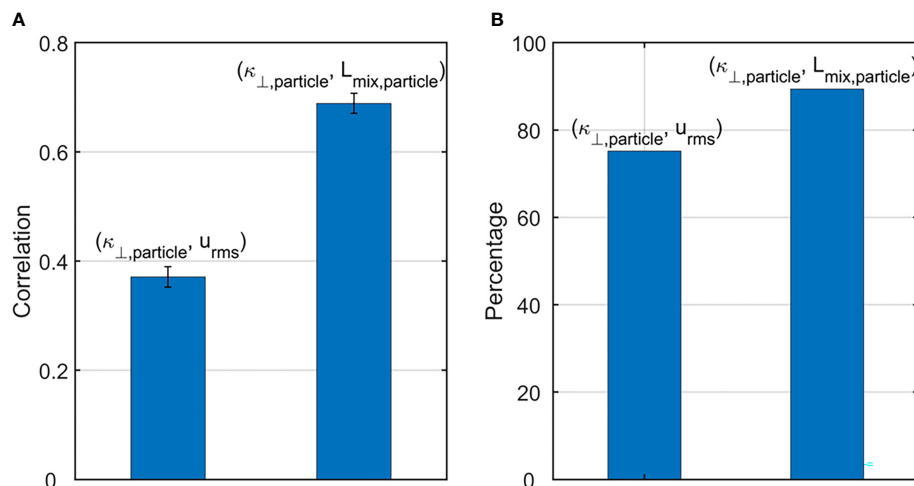


FIGURE 5

(A) The correlation coefficient of the global trends between $\kappa_{\perp,particle}$ and u_{rms} , and that between $\kappa_{\perp,particle}$ and $L_{mix,particle}$. The error bar is at the 95% confidence level by the bootstrapping method. (B) The percentage of the grid points where u_{rms} ($L_{mix,particle}$) and $\kappa_{\perp,particle}$ trends have the same sign.

The ratio of the relative trends between $L_{mix,particle}$ and $\kappa_{\perp,particle}$ is generally larger than that between u_{rms} and $\kappa_{\perp,particle}$ (Figures 7A, B). In 65% (73%) of the global ocean, the ratio of the relative trends between $L_{mix,particle}$ and $\kappa_{\perp,particle}$ relative trends is larger than 0.6 (0.5). We also evaluated the probability density functions (PDFs) of these ratios (Figures 7C, D). For the ratio between the $L_{mix,particle}$ and $\kappa_{\perp,particle}$ relative trends, the PDF is wide and asymmetric with a skewness value of 2.73 (Figure 7C). Its peak approximately occurs at 0.6. As to the ratio between the u_{rms} and $\kappa_{\perp,particle}$ relative trends, its PDF is only slightly asymmetric with a skewness value of 0.47 (Figure 7D). The PDF peak approximately occurs at 0.3. Comparing the two PDFs further reveal that $L_{mix,particle}$ plays a larger role than u_{rms} in modulating the relative trend of $\kappa_{\perp,particle}$.

3.2 Regional analysis

Considering that the mixing trend has complex spatial variability, next we focus on five representative regions to further characterize and interpret the mixing trend in the ocean (yellow boxes in Figure 3). All these five regions have statistically significant mixing trend (Figure 4A). They respectively represent areas with large positive mixing trends (Regions 3 and 5), weak positive mixing trend (Regions 1 and 4), and large negative mixing trend (Region 2). Region 3 is located in the equatorial Central Pacific, where the largest positive mixing trend occurs. Previous studies have shown that eddy mixing in the equatorial region is linked with the large-scale climate variability (e.g., El Niño-Southern Oscillation; Gnanadesikan et al., 2017; Busecke and Abernathy, 2019). Regions 1 and 4 are located in the mid-ocean regions in the Pacific. The mixing trend in these two regions are positive but weak. Region 5 is a representative patch in the Antarctic Circumpolar Current and mixing there is relatively strong and positive. There are also regions with negative mixing trends in the global oceans, for example Region 2.

The time series of the regionally averaged $\kappa_{\perp,particle}$ and the corresponding trends based on TS method are shown in Figure 4A. The trends in all the five regions are statistically significant at the 95% confidence level. In Region 2, the $\kappa_{\perp,particle}$ time series has a negative trend, decreasing by $1.62 \times 10^3 \text{ m}^2\text{s}^{-1}$ per decade. It accounts for 18.8% of the climate mean $\kappa_{\perp,particle}$. In all the other four regions, the $\kappa_{\perp,particle}$ time series have positive trends. Among these four regions, the trend in Region 3 is the largest, with a magnitude of $5.32 \times 10^3 \text{ m}^2\text{s}^{-1}$ per decade and accounting for 31.0% of the climate mean value. These results suggest that eddy mixing effect will be significantly enhanced in the context of tropical climate change.

We also carried out the mixing trend decomposition, based on Equation (6). In all these regions, the relative trend of $L_{mix,particle}$ has magnitude larger than that of u_{rms} (Figure 4B). The $L_{mix,particle}$ relative trend accounts for 56%-91% of the relative trend in $\kappa_{\perp,particle}$, indicating that $L_{mix,particle}$ contributes more than u_{rms} to the trend in $\kappa_{\perp,particle}$. On the other hand, the relative trends of both $L_{mix,particle}$ and u_{rms} are statistically significant at the 95% confidence level, except for the u_{rms} trend in Region 3.

To keep this study concise and reader-friendly, we only focus on five regions with significant mixing trends, located in either the Pacific Ocean or the Southern Ocean. Note, that, there are also regions in other basins with significant mixing trends, such as 39°N-57°N 10°W-20°W in the Atlantic Ocean. In this Atlantic box, the eddy diffusivity trend is $555.5 \text{ m}^2\text{s}^{-1}$ per decade. Consistent with the five regions we focus on, the $L_{mix,particle}$ relative trend in this box is also larger than that of u_{rms} (not shown).

4 Suppressed mixing length theory and its trend decomposition

Since eddy mixing length and eddy velocity magnitude jointly determine eddy diffusivity [Equation (5)], separately interpreting

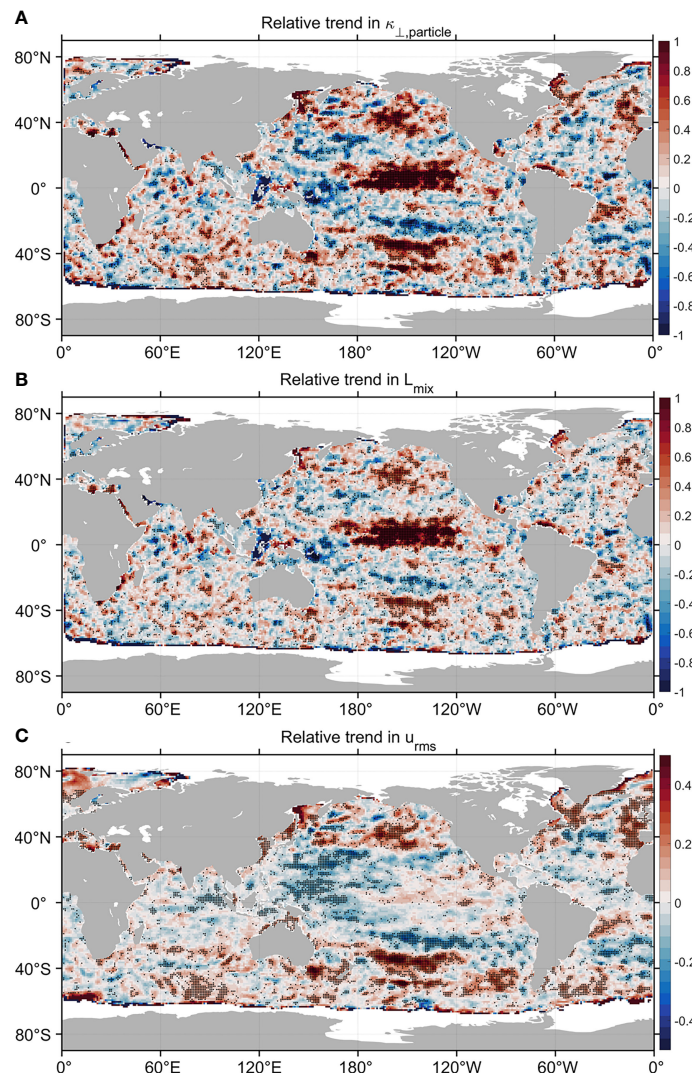


FIGURE 6

The relative trend of (A) $\kappa_{L,particle}$, (B) $L_{mix,particle}$, and (C) u_{rms} from Equation (6) in the global ocean during the period 1994–2017. Black dots indicate the grid points where the relative trend is statistically significant at the 95% confidence level.

the trends in mixing length and eddy velocity magnitude can help reveal the underlying mechanism of eddy mixing trend. We chose to use SMLT to discuss the mechanism of the trends in eddy mixing length (sections 4 and 5). In this section, we first introduce SMLT and then describe how to decompose the relative trend of SMLT-based mixing length into those of eddy and mean flow properties.

4.1 Suppressed mixing length theory

Though several mixing theories have been proposed (Ferrari and Nikurashin, 2010; Bates et al., 2014; Chen et al., 2015; Jansen et al., 2015; Wei and Wang, 2021), none of them can perfectly represent eddy mixing lengths. One of these theories that receive much attention is SMLT (Ferrari and Nikurashin, 2010), which is built on the critical layer idea from Green (1970). SMLT is derived based on several assumptions (e.g., linear, flat and homogeneous system, single-wave representation of eddies) (Ferrari and

Nikurashin, 2010; Chen et al., 2015) and it often breaks down at topographic regions (Naveira Garabato et al., 2011; Chen et al., 2014b). However, it successfully represent the mixing suppression phenomenon induced by the propagation of eddies relative to the mean flow (e.g., Ferrari and Nikurashin, 2010; Klocker et al., 2012b). Much evidence shows that SMLT can well capture the large-scale spatial structure of eddy mixing (e.g., Ferrari and Nikurashin, 2010; Klocker et al., 2012b; Abernathey and Marshall, 2013; Bates et al., 2014; Klocker and Abernathey, 2014; Roach et al., 2016; Roach et al., 2018; Groeskamp et al., 2020). In addition, SMLT-based eddy mixing was found to be linked with the large-scale climate variability (Busecke and Abernathey, 2019). Since this study focuses on the large-scale and long-term variability of eddy mixing, we chose to discuss the mechanism of the eddy mixing length trend using SMLT.

In brief, SMLT explicitly expresses the cross-stream eddy mixing length as a function of mean flow and eddy properties. Based on this theory, eddy mixing length in the cross-stream

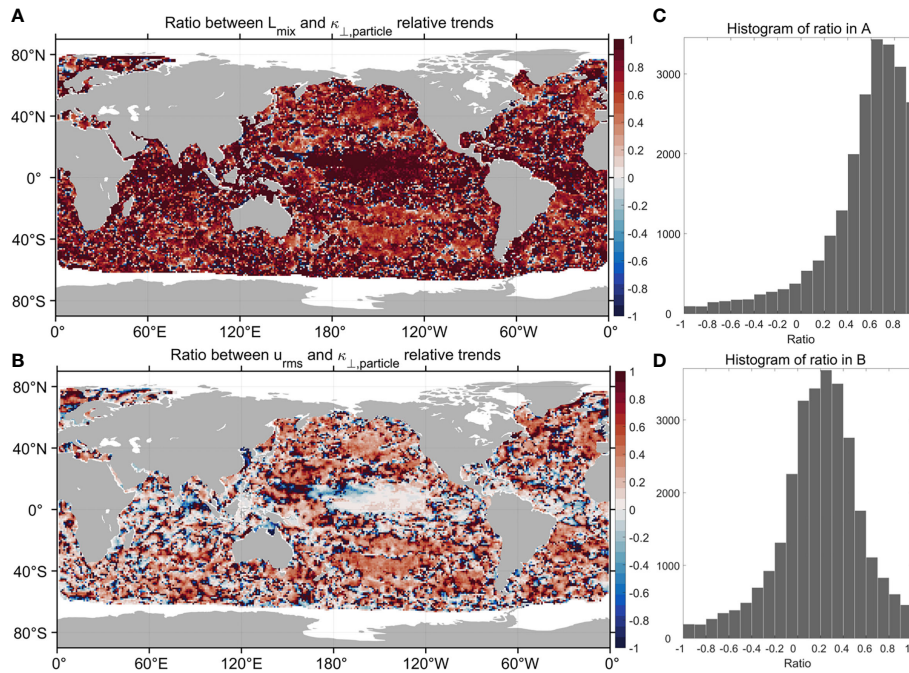


FIGURE 7 (A) The ratio of the relative trends between $L_{mix,particle}$ and $\kappa_{\perp,particle}$ in the global ocean. (B) The ratio of the relative trends between u_{rms} and $\kappa_{\perp,particle}$ in the global ocean. (C) and (D) show histograms of the ratios from panels A and B.

direction can be written as the product of eddy size L_{eddy} and a suppression factor S (≤ 1),

$$L_{mix,SMLT} = L_{eddy} \underbrace{\left[\frac{1}{1 + k_{eddy}^2 \gamma^{-2} (c_w - |U_g|)^2} \right]}_S \quad (7)$$

Following [Chen et al. \(2014b\)](#), L_{eddy} can be estimated from

$$L_{eddy}(x, y) = 2\pi \underbrace{\left[\frac{\iint S_{EKE}(k, l) dk dl}{\iint \sqrt{k^2 + l^2} S_{EKE}(k, l) dk dl} \right]}_{k_{eddy}^{-1}(x, y)}, \quad (8)$$

where k_{eddy} refers to the dominant eddy wavenumber, $S_{EKE}(k, l)$ is the wavenumber spectra of geostrophic EKE, k represents the zonal wavenumber, and l denotes the meridional wavenumber. The variable $|U_g|$ is the magnitude of the geostrophic mean flow and c_w represents the phase speed along the direction of geostrophic mean flow. Therefore, the term $c_w - |U_g|$ in the suppression factor S represents the propagating speed of eddies relative to the mean flow. The phase speed c_w is estimated from the Hovmöller diagram of sea surface height anomaly using the Radon transform method ([Guan et al., 2022](#)). As stated in [Chen et al. \(2014b\)](#), γ^{-1} represents the eddy decorrelation time scale,

$$\gamma(x, y) = \frac{u_{rms}(x, y)}{2\Gamma L_{eddy}(x, y)}. \quad (9)$$

All these parameters above are diagnosed using AVISO data.

Based on Equations (7)–(9), we can obtain another expression of SMLT,

$$L_{mix,SMLT} = L_{eddy} \underbrace{\left[\frac{1}{1 + 16\pi^2 \Gamma^2 u_{rms}^{-2} (c_w - |U_g|)^2} \right]}_S \quad (10)$$

Similar to Equation (5), based on the mixing length theory ([Taylor, 1915](#)), we can diagnose the SMLT-based cross-stream eddy diffusivity from

$$\kappa_{\perp,SMLT} = \Gamma u_{rms} L_{mix,SMLT}. \quad (11)$$

4.2 Decomposition of eddy mixing length trends

Equation (10) shows that the SMLT-based eddy mixing length is mainly regulated by the following three terms: L_{eddy} , u_{rms} and $c_w - |U_g|$. We can explore their respective contribution to the trend of eddy mixing length using the trend decomposition method from [Guo et al. \(2022\)](#). Note that this decomposition method has also been used in section 3.1.2. The SMLT-based eddy mixing length ($L_{mix,SMLT,2}$) trend can be decomposed as follows:

$$\frac{1}{L_{mix,SMLT}} \frac{\partial L_{mix,SMLT}}{\partial t} = \frac{1}{L_{eddy}} \frac{\partial L_{eddy}}{\partial t} + \underbrace{\frac{2(1-S)}{u_{rms}} \frac{\partial u_{rms}}{\partial t}}_{S1} \underbrace{\frac{2(1-S)}{(c_w - |U_g|)} \frac{\partial (c_w - |U_g|)}{\partial t}}_{S2}, \quad (12)$$

$\frac{1}{S} \frac{\partial S}{\partial t}$

where S1 and S2 represent the contributions of u_{rms} and $c_w - |U_g|$ to the trend of eddy mixing length. Equation (12) reveals that

the relative trend of $L_{mix,SMLT}$ can be represented in the form of the sum of the relative trends of these three terms (L_{eddy} , $S1$, and $S2$). Note that $S1$ represents the contribution of u_{rms} to the $L_{mix,SMLT}$ trend. Therefore, u_{rms} can not only directly affect the eddy diffusivity trend [Equation (6)], but also indirectly modulate the eddy diffusivity trend by influencing the eddy mixing length [Equation (12)].

Based on Equation (12), one can assess the contribution of each factor (L_{eddy} , $S1$, and $S2$) to the trend of the SMLT-based eddy mixing length. In the regions where SMLT successfully captures the trend in particle-based eddy mixing lengths, these results based on Equation (12) can help interpret the particle-based eddy mixing length trend as well.

5 Interpreting trends in eddy mixing length

5.1 Trend decomposition of eddy mixing length

We compare the SMLT-based trends in eddy diffusivity and mixing length with those from particles (Figure 8). SMLT can not capture the magnitude of the trend in eddy diffusivity. Also, SMLT does not capture the magnitude of the trend in eddy mixing length. This result is to a certain degree consistent with Guan et al. (2022), who found that the SMLT-based eddy diffusivity magnitude is noticeably smaller than its particle-based counterpart. The trend sign of the SMLT-based eddy diffusivity is consistent with the particle-based result in all the regions, except for Region 3. Concerning the trend in eddy mixing length, SMLT- and particle-based results have consistent signs in Regions 4 and 5. In the other three regions, the trend of the SMLT-based eddy mixing length is insignificant, whereas those from particles are significant. Therefore, SMLT could be used to reveal the mechanism of the $L_{mix,particle}$ trend in only Regions 4 and 5.

The decomposition of the $L_{mix,SMLT}$ trend, based on Equation (12), reveals that among the three factors (L_{eddy} , u_{rms} , and $c_w - |U_g|$),

u_{rms} plays a dominant role in determining the trend in $L_{mix,SMLT}$. On the other hand, the trend in $c_w - |U_g|$ plays a negative role in the trend of eddy mixing length. As shown in Figure 9, in all the five regions, the relative trend in term $S1$ is larger than those in $S2$ and L_{eddy} . Note that $S1$ represents the contribution of u_{rms} to the $L_{mix,SMLT}$ trend. Therefore, besides acting as a direct and important governor of the eddy diffusivity trend (Figure 4B), u_{rms} also play an indirect role in modulating eddy diffusivity trend through influencing the eddy mixing length (Figure 9). Although the relative trends of L_{eddy} and $S1$ have comparable magnitudes in Region 3, the relative trend of L_{eddy} is much smaller than that of $S1$ in the other regions, indicating a relative small role of L_{eddy} in influencing the $L_{mix,SMLT}$ trend. In all the regions except Region 3, the sign of the relative trend in $S2$ is opposite to that of $L_{mix,SMLT}$. Therefore, in these regions, $c_w - |U_g|$ plays a negative role in the trend of eddy mixing length. Considering that the SMLT-based and particle-based eddy mixing lengths have the same trend sign in Regions 4 and 5, the SMLT results in these two regions can, to a certain degree, indicate the underlying mechanism of the particle-based eddy mixing length trend. However, in the other three regions (Regions 1-3), the sign of the trend in SMLT-based mixing length differs from that of particle-based mixing length. Therefore, SMLT cannot be used to explain mixing-length trends in Regions 1-3.

Here we compare the trends in eddy properties with the mixing trends (Figure 10). In all the selected regions, the trend in eddy size (L_{eddy}) has the same sign as the trends in the particle-based eddy mixing length ($L_{mix,particle}$) and eddy diffusivity ($\kappa_{\perp,particle}$). This indicates that a positive response of the long-term variation of $L_{mix,particle}$ and $\kappa_{\perp,particle}$ to the variability in L_{eddy} . However, though the trend in $c_w - |U_g|$ also has consistent sign with those in $L_{mix,particle}$ and $\kappa_{\perp,particle}$ in all the regions except Region 3 (Figure 10B), $c_w - |U_g|$ and L_{eddy} play opposite roles in shaping the mixing trends [see Equation (12)]. Similarly, in all these regions, the trend signs of u_{rms} are consistent with those of $L_{mix,particle}$ and $\kappa_{\perp,particle}$ (Figure 9C). This indicates that u_{rms} plays a positive role in the mixing trends, consistent with the mixing length theory [Equation(5)] and SMLT [Equation (10)].

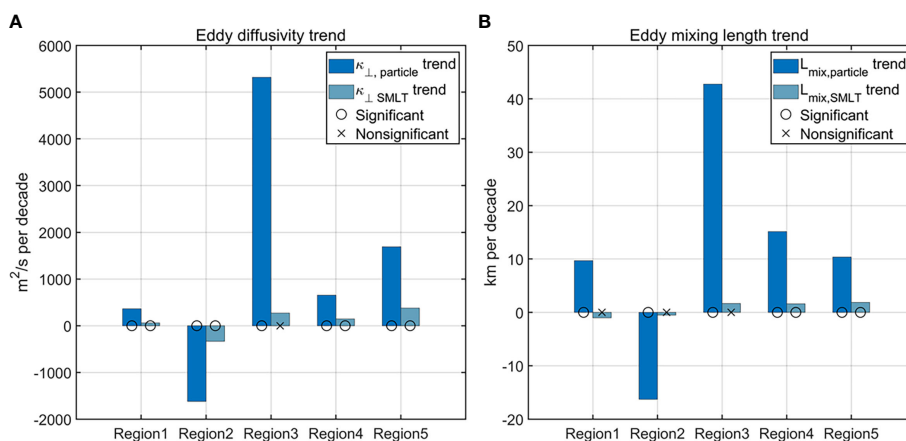


FIGURE 8

Trends in (A) eddy diffusivity and (B) eddy mixing length from the particle-based and SMLT-based methods in the representative regions shown in Figure 3. Statistically insignificant trends at the 95% confidence level are marked by "x", and significant trends are marked by "o".

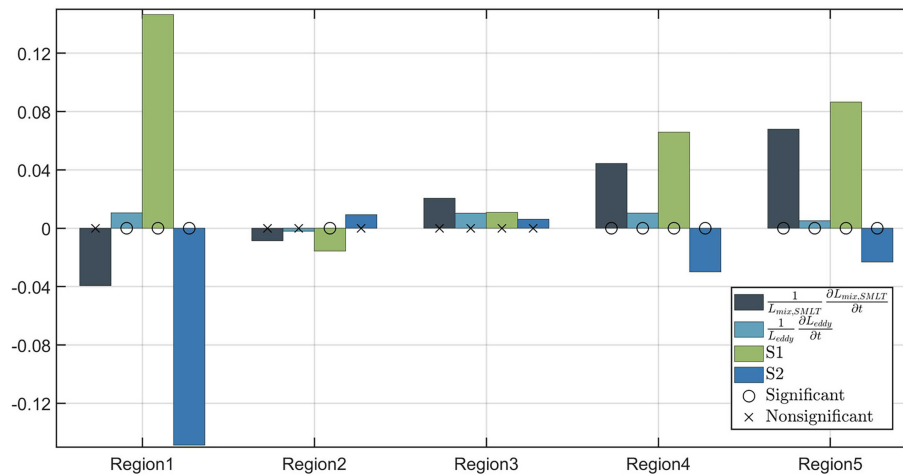


FIGURE 9 The relative trends of $L_{mix,SMLT}$, L_{eddy} , $S1$, and $S2$ from Equation (12) in the representative regions. The trends that are statistically insignificant at the 95% confidence level are marked by "x", and those significant ones are marked by "o".

5.2 Trends in eddy/mean flow properties

We further depict the regional trends in the eddy flow properties that are linked with the SMLT-based eddy diffusivity: Eddy size (L_{eddy}), the propagating speed of eddies relative to the mean flow ($c_w - |U_g|$), eddy velocity magnitude (u_{rms}) and the inverse of the eddy decorrelation time scale (γ) (Figure 10). In Regions 1, 4 and 5, eddy gets larger, more energetic, and propagate faster relative to the mean flow during the period 1997-2017. However, in these three regions, the inverse of the eddy decorrelation time scale has an increasing trend, indicating a faster decay of eddies during this period. In contrast, in Region 2, eddies get less energetic and decay more slowly during this time period. Yet, the trends in eddysize and eddy propagating speed relative to the mean flow are statistically nonsignificant. In Region 3, however, there are no statistically significant trends in all the four eddy properties.

Note that our trends in eddy properties can be interpreted based on previous studies about eddy dynamics. Firstly, we found that faster (slower) propagating speed of eddies relative to the mean flow generally corresponds to smaller (larger) eddy decorrelation time scale, i.e., faster (slower) eddy decay (Figures 10B, D). This phenomenon is consistent with the observation finding by Liu et al. (2022). Through both observations and idealized experiments, they demonstrate that a stronger Rossby wave phase speed leads to fast radiation of eddy energy and thus shorter eddy lifespan. Secondly, faster (slower) propagating speed of eddies relative to the mean flow often corresponds larger (smaller) eddy size. Specifically, in Regions 1, 4 and 5, the trends in $c_w - |U_g|$ and L_{eddy} are both statistically significant and they have the same signs. This is to a certain extent related to the following previous findings. Klocker and Marshall (2014) found that eddy phase speed is generally consistent with the phase speed of linear, long Rossby waves that are Doppler shifted with the barotropic mean flow.

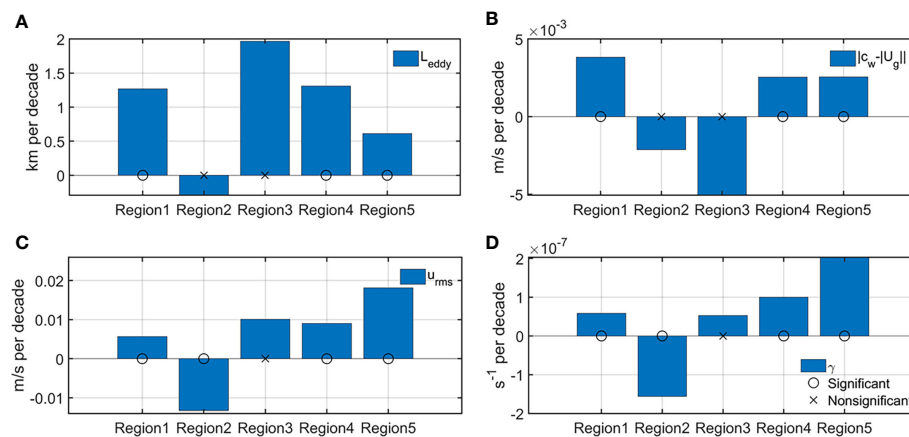


FIGURE 10 Trends of eddy/mean flow parameters from SMLT in the representative regions shown in Figure 3. (A) L_{eddy} . (B) $|c_w - |U_g||$. (C) u_{rms} . (D) γ . The trends that are statistically insignificant at the 95% confidence level are marked by "x", and those significant ones are marked by "o".

Specifically, they show that the eddy propagation speed relative to the barotropic mean flow is βL_D^2 , where L_D is the Rossby deformation radius. In general, L_D can be an approximate substitute for L_{eddy} (Tulloch et al., 2011; Klocker and Abernathy, 2014). Therefore, it is unsurprising that $c_w - |U_g|$ has consistent trend sign with L_{eddy} . One caveat of this interpretation is that U_g here is the surface geostrophic mean flow magnitude, not the barotropic mean flow considered in Klocker and Marshall (2014).

6 Interpreting trends in eddy velocity magnitude

Mixing length theory indicates that eddy diffusivity is proportional to the product of eddy mixing length and eddy velocity magnitude u_{rms} [Equation (5)]. Here we interpret the trends in u_{rms} using the geostrophic EKE budget, which is a key step towards unravelling the mechanism of the mixing-length trend.

6.1 Geostrophic EKE budget

To investigate the mechanism of the trend in u_{rms} (surface geostrophic eddy velocity magnitude), we chose to derive and diagnose the budget equation of the surface geostrophic EKE (for details, see [Supplementary Material](#)). The formulation of the framework is inspired by the eddy/mean energy diagnostic framework from Chen et al. (2014a). But different from Chen et al. (2014a), our derivation here separately considers the geostrophic and ageostrophic EKE,

$$\frac{\partial \overline{K_{E,g}}}{\partial t} = ADV_g + M_{K_{E,g}} + PW_H + R. \quad (13)$$

Here $K_{E,g}$ refers to the geostrophic EKE

$$K_{E,g} = \frac{1}{2} \rho_0 \overline{(u_g'^2 + v_g'^2)}, \quad (14)$$

where ρ_0 is the sea surface density and takes a constant of 1027.5 kg m^{-3} . The overbar refers to the annual-mean over each year and $'$ denotes the deviation from the mean.

The mathematical formulas and the physical meanings of the terms on the right-hand side of Equation (13) are provided in [Table 1](#). Equation (13) indicates that the trend in the geostrophic EKE may be induced by geostrophic advection (ADV_g), the geostrophic contribution to the eddy-mean kinetic energy exchange rate ($M_{K_{E,g}}$), the pressure work due to the horizontal ageostrophic flow (PW_H) and the residual term (R). As shown in [Table 1](#), the residual term, R , includes four components: energy advection related to ageostrophic flow (ADV_r), the contribution of ageostrophic flow to the eddy-mean kinetic energy exchange rate ($M_{K_{E,r}}$), the change of EKE due to vertical and horizontal friction (X_{K_E}), and the temporal change rate of $K_{E,r}$. Among these components, ADV_r , $M_{K_{E,r}}$ and $\frac{\partial \overline{K_{E,r}}}{\partial t}$ can be diagnosed from

$$ADV_r = - \underbrace{\nabla_H (\mathbf{u}_o \cdot 0.5 \rho_0 \overline{(u_o'^2 + v_o'^2)})}_{ADV_o} - ADV_g, \quad (15)$$

$$M_{K_{E,r}} = - \underbrace{\rho_0 \overline{(\mathbf{u}_o' \cdot \nabla_H \bar{\mathbf{u}}_o + \mathbf{v}_o' \cdot \nabla_H \bar{\mathbf{v}}_o)}}_{M_{K_{E,o}}} - M_{K_{E,g}}, \quad (16)$$

$$\frac{\partial \overline{K_{E,r}}}{\partial t} = \frac{\partial \left[\frac{1}{2} \rho_0 \overline{(u_o'^2 + v_o'^2)} \right]}{\partial t} - \frac{\partial \overline{K_{E,g}}}{\partial t}. \quad (17)$$

Here u_o and v_o refer to the total surface velocity in the zonal and meridional direction. The ageostrophic velocity is defined as the difference between the total surface velocity and the geostrophic velocity,

$$\mathbf{u}_{ag} = \mathbf{u}_o - \mathbf{u}_g. \quad (18)$$

The full velocity u_o is available from the OSCAR dataset, and the geostrophic velocity u_g and sea surface height η are available from the AVISO dataset. Therefore, one can directly diagnose all the terms in Equation (13) except for the R term. Then we can approximately infer the value of R by closing the $K_{E,g}$ budget. Concerning the terms in the R equation ([Table 1](#)), using OSCAR and AVISO data, we can directly diagnose ADV_r , $M_{K_{E,r}}$ and $\frac{\partial \overline{K_{E,r}}}{\partial t}$. The X term is not explicitly diagnosed due to the absence of observed horizontal/vertical friction information.

6.2 Geostrophic EKE budget trends

To explore the origin of the trends in the surface geostrophic EKE and thus u_{rms} , we diagnosed the geostrophic EKE budget for each year [Equation (13)]. Then we estimated the trends in each term during the period 1994–2017. As shown in [Figure 11](#), in all selected regions, the trends of ADV_g and $M_{K_{E,g}}$ are generally small, with magnitudes on the order of $10^{-7} \sim 10^{-8} \text{ J m}^{-3}$. In contrast, the trends in PW_H and R are on the order of $10^{-5} \sim 10^{-6} \text{ J m}^{-3}$, much larger than those in ADV_g and $M_{K_{E,g}}$. Therefore, in these five representative regions, the trends in the surface geostrophic EKE are mainly induced by the pressure work due to the horizontal ageostrophic flow (PW_H) and the residual term (R).

The trends in PW_H are statistically significant at the 95% confidence level in Regions 4 and 5. In these two regions, the trends in PW_H and u_{rms} have consistent signs ([Figures 10C, 11C](#)). Therefore, in Regions 4 and 5, the trend in pressure work (PW_H) contributes to the trend in u_{rms} . Using the classical linear Ekman theory, we express PW_H as a function of wind stress and geostrophic flow (see [Supplementary Material 3](#) for details). A series of studies have shown that both wind speed and ocean currents are accelerating (Hu et al., 2020; Peng et al., 2022). Much evidence have demonstrated that the increasing trend of EKE in the Southern Ocean is associated with enhanced wind stress (Sallee et al., 2011; Hogg et al., 2015; Mudelsee, 2019; Cai et al., 2022). In our study, Regions 4 and 5 are within the Southern Ocean. Similarly, in the western boundary current regions, Beal and Elipot (2016) found that the enhanced wind power leads to the strengthening of EKE. Therefore, the acceleration of the wind and the geostrophic flow may jointly induce the trend in the pressure work (PW_H).

TABLE 1 The mathematical formulas and physical meanings of the terms on the right hand side of Equation (13).

Term	Mathematical form	Meaning
ADV_g	$-\nabla_H(\overline{u_g \cdot K_{Eg}})$	The change rate of geostrophic EKE due to geostrophic advection
$M_{K_{Eg}}$	$-\rho_0(\overline{u'_g \cdot u'_g} \cdot \nabla_H \overline{u_g} + \overline{v'_g \cdot v'_g} \cdot \nabla_H \overline{v_g})$	The change rate of geostrophic EKE induced by the geostrophic eddy momentum flux
PW_H	$-\overline{u'_{ag} \cdot \nabla_H p'} \approx -g\rho_0 \overline{u'_{ag} \cdot \nabla_H \eta'}$	The pressure work induced by ageostrophic flow
R	$ADV_r + M_{K_{Er}} + X_{K_E} - \frac{\partial \overline{K_{Er}}}{\partial t}$	The residual term

∇_H is the two-dimensional divergence operator, the subscript $g(ag)$ represents the sea surface geostrophic (ageostrophic) flow. The term ρ is sea surface density, p is sea surface pressure, and η is sea surface height. The definition of the subterms in the R formula is available in Equations (15)–(17). For details, see [Supplementary Material](#).

Using the OSCAR and AVISO datasets, we also diagnosed the energy terms in the R equation (Table 1). We estimated the ADV_r and $M_{K_{Er}}$ terms [Equations (15) and (16)], which are the part of the advection and eddy-mean energy exchange rate terms related to ageostrophic flow. The term X_{K_E} is inferred from the other terms in the R equation (Table 1). In all the five regions, the trends in both ADV_r and $M_{K_{Er}}$ are on the order of 10^{-7} – 10^{-8} J m⁻³, whereas the trend in X_{K_E} is on the order of 10^{-5} – 10^{-6} J m⁻³ (not shown). Therefore, the leading contributor to the trend in R is X_{K_E} , which denotes the EKE change rate due to horizontal/vertical friction. One caveat, however, is that uncertainties exist in our estimation of X_{K_E} . Example sources of uncertainty are provided next. One, our derivation of the geostrophic EKE budget [Equation (13)] ignores the contribution of vertical velocity to advection and eddy-mean energy exchange terms. Furthermore, the gridded AVISO dataset averages out the high-frequency ocean motions (e.g., internal tides). These issues would lead to uncertainties in our inference of R . In addition, the ageostrophic flow from OSCAR is to a large extent the Ekman flow and thus it does not include the submesoscale component of the ageostrophic flow. In consequence, our estimation of ADV_r , $M_{K_{Er}}$ and $\frac{\partial \overline{K_{Er}}}{\partial t}$ excludes the contribution of oceanic submesoscales, which may be non-negligible. The estimates of R and X_{K_E} terms could be improved as the resolution of satellite observation increases. Further investigation along this line is left for future work.

7 Conclusion

Using the AVISO observations during 1994–2017, this study estimated the trend in particle-based eddy diffusivity ($\kappa_{\perp,particle}$) at the global surface ocean. The spatial structure of this eddy mixing trend has large regional variability. In 54% of the global ocean, $\kappa_{\perp,particle}$ shows an increasing trend. The globally integrated $\kappa_{\perp,particle}$ shows a significant increasing trend, with an increase of 284.1 m²s⁻¹ per decade, accounting for 3.7% of the climate mean value. Using a trend decomposition method (Guo et al., 2022) and the mixing length theory, we found that the relative trend of $\kappa_{\perp,particle}$ is equal to the sum of the relative trend in eddy mixing length (L_{mix}) and that of eddy velocity magnitude (u_{rms}). In 73% of the global ocean, L_{mix} contributes more to the relative trend in eddy diffusivity than u_{rms} . Therefore, in these regions, the main direct source of the $\kappa_{\perp,particle}$ trend is the trend in L_{mix} , not that in u_{rms} . Yet, the contribution of u_{rms} is also noticeable.

Since L_{mix} and u_{rms} jointly determine eddy diffusivity, we explore the mechanism of eddy mixing trends by interpreting the trends in L_{mix} and u_{rms} , respectively. We chose to discuss the mechanism of the L_{mix} trend using SMLT and its trend decomposition. SMLT well captures the trend sign of the particle-based eddy mixing lengths in two of the five regions, i.e., Regions 4 and 5. The trends in eddy/mean flow parameters related to SMLT (e.g., eddy size, u_{rms} , the propagating speed of eddies relative to the mean flow, and the inverse of the eddy decorrelation time scale) jointly determine the

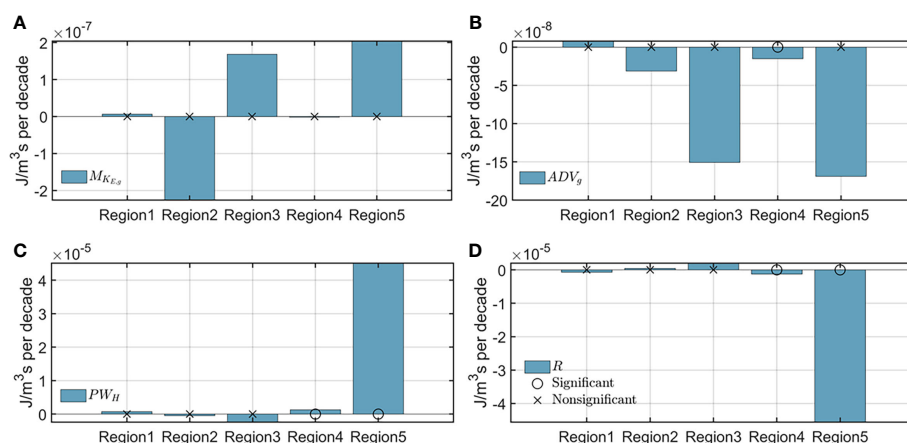


FIGURE 11 The trend in each term from the geostrophic EKE budget [Equation (13)] in the representative regions. (A) $M_{K_{Eg}}$. (B) ADV_g . (C) PW_H . (D) R . Statistically insignificant trends at the 95% confidence level are marked by "x", and significant trends are marked by "o".

trend in the SMLT-based mixing length. Among these parameters, u_{rms} plays a dominant role in determining the SMLT-based L_{mix} trend. We also found that u_{rms} dose not only directly modulate the trend in eddy mixing, but also indirectly affect the eddy diffusivity trend through its link with the L_{mix} .

We then discuss the trend in u_{rms} , which also help unravel the origin of the eddy mixing trend. By diagnosing a novel surface geostrophic EKE budget, we found that pressure work due to the horizontal ageostrophic flow plays a dominant role in the trend in u_{rms} . Then using the classical linear Ekman theory, we developed a formula linking pressure work with wind stress and geostrophic flow. This formula and evidence in literature (e.g., Sallee et al., 2011; Hogg et al., 2015; Mudelsee, 2019; Hu et al., 2020; Cai et al., 2022; Peng et al., 2022) suggests that the acceleration of wind and geostrophic flow might jointly induce the trend in pressure work.

There are potential avenues to further improve this work. One, this study focuses on the surface ocean. The mixing trend at mid-depths and in the deep ocean remains unclear. Also it would be worthwhile evaluating whether this observed mixing trend is well captured in the widely-used numerical products (Ma et al., 2010; Yang et al., 2018; Xu et al., 2021). Two, the mechanisms of the trends in relevant eddy properties (e.g., eddy size and eddy phase speed) need to be further explored. This effort would help design eddy parameterization schemes taking into account mixing trend.

One caveat of this work is that uncertainties remain in our mixing trend estimation. The data duration we use is only 24 years and a longer time series may lead to a more robust estimation of the long-term trend (Beech et al., 2022). Therefore, though expensive, continuous observations of the oceanic currents and other relevant tracer variables (e.g., temperature) would be valuable for more accurate trend estimation.

Despite the uncertainties in our trend estimation, our results clearly indicate that there is regional long-term adjustment of mesoscale eddies throughout the ocean. As the ocean's response to climate change is slow, ocean changes, including the changes in eddy mixing, will continue building up. The eddy adjustment may significantly affect the distribution of key tracers in the ocean (e.g., heat, salt, and nutrient) and thus change the water mass distribution and air-sea interaction. This in turn would lead to the variability of the ocean circulation, climate system and marine ecosystem. Therefore, it could be useful to fully consider the long-term trends in eddy mixing when implementing eddy parameterization schemes in non-eddy-resolving climate models.

Data availability statement

The original contributions presented in the study are included in the article/Supplementary Material. Further inquiries can be directed to the corresponding author.

References

Abernathey, R. P., and Marshall, J. (2013). Global surface eddy diffusivities derived from satellite altimetry. *J. Geophys. Res.: Oceans* 118, 901–916. doi: 10.1002/jgrc.20066

Author contributions

RC and GZ conceived this project. RC conducted the particle-tracking experiments and formulated the diagnosis frameworks. GZ analyzed the data and wrote the initial draft. RC, LL, HW and SS reviewed and revised the manuscript. All authors interpreted the results and approved the submitted version.

Funding

This work was supported by the National Natural Science Foundation of China through 42076007. LL is partially supported by the seed grant from the Institute of Computational and Data Sciences at the Pennsylvania State University.

Acknowledgments

We thank Wenting Guan for her technical assistance about eddy diffusivity estimates, and Qianqian Geng for proofreading and editing the manuscript. h T. Gille and Julie L. McClean from Scripps Institution of Oceanography at the University of California, San Diego for introducing us to the topic of Lagrangian eddy diffusivities.

Conflict of interest

The authors declare that the research was conducted in the absence of any commercial or financial relationships that could be construed as a potential conflict of interest.

Publisher's note

All claims expressed in this article are solely those of the authors and do not necessarily represent those of their affiliated organizations, or those of the publisher, the editors and the reviewers. Any product that may be evaluated in this article, or claim that may be made by its manufacturer, is not guaranteed or endorsed by the publisher.

Supplementary material

The Supplementary Material for this article can be found online at: <https://www.frontiersin.org/articles/10.3389/fmars.2023.1157049/full#supplementary-material>

Abernathey, R., Marshall, J., and Ferreira, D. (2011). The dependence of southern ocean meridional overturning on wind stress. *J. Phys. Oceanogr.* 41, 2261–2278. doi: 10.1175/JPO-D-11-023.1

- Bates, M., Tulloch, R., Marshall, J., and Ferrari, R. (2014). Rationalizing the spatial distribution of mesoscale eddy diffusivity in terms of mixing length theory. *J. Phys. Oceanogr.* 44, 1523–1540. doi: 10.1175/JPO-D-13-0130.1
- Beal, L. M., and Elipot, S. (2016). Broadening not strengthening of the agulhas current since the early 1990s. *Nature* 540, 570–573. doi: 10.1038/nature19853
- Beech, N., Rackow, T., Semmler, T., Danilov, S., Wang, Q., and Jung, T. (2022). Long-term evolution of ocean eddy activity in a warming world. *Nat. Climate Change* 12, 910–917. doi: 10.1038/s41558-022-01478-3
- Bolton, T., Abernathy, R., and Zanna, L. (2019). Regional and temporal variability of lateral mixing in the north Atlantic. *J. Phys. Oceanogr.* 49, 2601–2614. doi: 10.1175/JPO-D-19-0042.1
- Bonjean, F., and Lagerloef, G. S. (2002). Diagnostic model and analysis of the surface currents in the tropical Pacific ocean. *J. Phys. Oceanogr.* 32, 2938–2954. doi: 10.1175/1520-0485(2002)032<2938:DMAAOT>2.0.CO;2
- Busecke, J. J., and Abernathy, R. P. (2019). Ocean mesoscale mixing linked to climate variability. *Sci. Adv.* 5, eaav5014. doi: 10.1126/sciadv.aav5014
- Busecke, J., Abernathy, R. P., and Gordon, A. L. (2017). Lateral eddy mixing in the subtropical salinity maxima of the global ocean. *J. Phys. Oceanogr.* 47, 737–754. doi: 10.1175/JPO-D-16-0215.1
- Cai, Y., Chen, D., Mazloff, M. R., Lian, T., and Liu, X. (2022). Topographic modulation of the wind stress impact on eddy activity in the southern ocean. *Geophys. Res. Lett.* 49, e2022GL097859. doi: 10.1029/2022GL097859
- Chen, R., Flierl, G. R., and Wunsch, C. (2014a). A description of local and nonlocal eddy-mean flow interaction in a global eddy-permitting state estimate. *J. Phys. Oceanogr.* 44, 2336–2352. doi: 10.1175/JPO-D-14-0009.1
- Chen, R., Gille, S. T., and McClean, J. L. (2017). Isopycnal eddy mixing across the kuroshio extension: stable versus unstable states in an eddy model. *J. Geophys. Res.: Oceans* 122, 4329–4345. doi: 10.1002/2016JC012164
- Chen, R., Gille, S., McClean, J., Flierl, G., and Griesel, A. (2015). A multiwavenumber theory for eddy diffusivities and its application to the southeast Pacific (DIMES) region. *J. Phys. Oceanogr.* 45, 1877–1896. doi: 10.1175/JPO-D-14-0229.1
- Chen, G., Li, Y., Xie, Q., and Wang, D. (2018). Origins of eddy kinetic energy in the bay of Bengal. *J. Geophys. Res.: Oceans* 123, 2097–2115. doi: 10.1002/2017JC013455
- Chen, R., McClean, J. L., Gille, S. T., and Griesel, A. (2014b). Isopycnal eddy diffusivities and critical layers in the kuroshio extension from an eddy ocean model. *J. Phys. Oceanogr.* 44, 2191–2211. doi: 10.1175/JPO-D-13-0258.1
- Chen, R., and Waterman, S. (2017). Mixing nonlocality and mixing anisotropy in an idealized western boundary current jet. *J. Phys. Oceanogr.* 47, 3015–3036. doi: 10.1175/JPO-D-17-0011.1
- Chernick, M. R. (2011). *Bootstrap methods: a guide for practitioners and researchers* (John Wiley & Sons).
- Church, J. A., White, N. J., Konikow, L. F., Domingues, C. M., Cogley, J. G., Rignot, E., et al. (2011). Revisiting the earth's sea-level and energy budgets from 1961 to 2008. *Geophys. Res. Lett.* 38 (18), L18601. doi: 10.1029/2011GL048794
- Danabasoglu, G., and Marshall, J. (2007). Effects of vertical variations of thickness diffusivity in an ocean general circulation model. *Ocean Model.* 18, 122–141. doi: 10.1016/j.ocemod.2007.03.006
- Davis, R. E. (1987). Modeling eddy transport of passive tracers. *J. Mar. Res.* 45, 635–666. doi: 10.1357/00224087788326803
- Davis, R. E. (1991). Observing the general circulation with floats. *Deep Sea Res. Part A. Oceanogr. Res. Pap.* 38, 531–571. doi: 10.1016/S0198-0149(12)80023-9
- Dohan, K. (2017). Ocean surface currents from satellite data. *J. Geophys. Res.: Oceans* 122, 2647–2651. doi: 10.1002/2017JC012961
- Du, Y., Zhang, Y., Feng, M., Wang, T., Zhang, N., and Wijffels, S. (2015). Decadal trends of the upper ocean salinity in the tropical Indo-Pacific since mid-1990s. *Sci. Rep.* 5, 1–9. doi: 10.1038/srep16050
- Ferrari, R., and Nikurashin, M. (2010). Suppression of eddy diffusivity across jets in the southern ocean. *J. Phys. Oceanogr.* 40, 1501–1519. doi: 10.1175/2010JPO4278.1
- Ferrari, R., and Wunsch, C. (2009). Ocean circulation kinetic energy: reservoirs, sources, and sinks. *Annu. Rev. Fluid Mech.* 41, 253–282. doi: 10.1146/annurev.fluid.40.111406.102139
- Fox-Kemper, B., Adcroft, A., Böning, C. W., Chassignet, E. P., Curchitser, E., Danabasoglu, G., et al. (2019). Challenges and prospects in ocean circulation models. *Front. Mar. Sci.* 6, 65. doi: 10.3389/fmars.2019.00065
- Gent, P. R., and McWilliams, J. C. (1990). Isopycnal mixing in ocean circulation models. *J. Phys. Oceanogr.* 20, 150–155. doi: 10.1175/1520-0485(1990)020<0150:IMIOCM>2.0.CO;2
- Gnanadesikan, A., Pradal, M., and Abernathy, R. (2015). Isopycnal mixing by mesoscale eddies significantly impacts oceanic anthropogenic carbon uptake. *Geophys. Res. Lett.* 42, 4249–4255. doi: 10.1002/2015GL064100
- Gnanadesikan, A., Russell, A., Pradal, M. A., and Abernathy, R. (2017). Impact of lateral mixing in the ocean on El Niño in a suite of fully coupled climate models. *J. Adv. Model. Earth Syst.* 9, 2493–2513. doi: 10.1002/2017MS000917
- Gocic, M., and Trajkovic, S. (2013). Analysis of changes in meteorological variables using Mann-Kendall and Sen's slope estimator statistical tests in Serbia. *Global Planet. Change* 100, 172–182. doi: 10.1016/j.gloplacha.2012.10.014
- Green, J. S. A. (1970). Transfer properties of the large-scale eddies and the general circulation of the atmosphere. *Q. J. R. Meteorol. Soc.* 96, 157–185. doi: 10.1002/qj.49709640802
- Griesel, A., Gille, S. T., Sprintall, J., McClean, J. L., Lacasce, J. H., and Maltrud, M. E. (2010). Isopycnal diffusivities in the Antarctic circumpolar current inferred from Lagrangian floats in an eddy model. *J. Geophys. Res.: Oceans* 115, C06006. doi: 10.1029/2009JC005821
- Griesel, A., McClean, J. L., Gille, S. T., Sprintall, J., and Eden, C. (2014). Eulerian and Lagrangian isopycnal eddy diffusivities in the southern ocean of an eddy model. *J. Phys. Oceanogr.* 44, 644–661. doi: 10.1175/JPO-D-13-039.1
- Griffies, S. M. (1998). The Gent-McWilliams skew flux. *J. Phys. Oceanogr.* 28, 831–841. doi: 10.1175/1520-0485(1998)028<0831:TGMSPF>2.0.CO;2
- Groeskamp, S., LaCasce, J. H., McDougall, T. J., and Rogé, M. (2020). Full-depth global estimates of ocean mesoscale eddy mixing from observations and theory. *Geophys. Res. Lett.* 47, e2020GL089425. doi: 10.1029/2020GL089425
- Guan, W., Chen, R., Zhang, H., Yang, Y., and Wei, H. (2022). Seasonal surface eddy mixing in the kuroshio extension: estimation and machine learning prediction. *J. Geophys. Res.: Oceans* 127, e2021JC017967. doi: 10.1029/2021JC017967
- Guo, Y., Bachman, S., Bryan, F., and Bishop, S. (2022). Increasing trends in oceanic surface poleward eddy heat flux observed over the past three decades. *Geophys. Res. Lett.* 49, e2022GL099362. doi: 10.1029/2022GL099362
- Hamed, K. H., and Rao, A. R. (1998). A modified Mann-Kendall trend test for autocorrelated data. *J. Hydrol.* 204, 182–196. doi: 10.1016/S0022-1694(97)00125-X
- Hogg, A. M., Meredith, M. P., Chambers, D. P., Abrahamson, E. P., Hughes, C. W., and Morrison, A. K. (2015). Recent trends in the southern ocean eddy field. *J. Geophys. Res.: Oceans* 120, 257–267. doi: 10.1002/2014JC010470
- Hu, S., Sprintall, J., Guan, C., McPhaden, M. J., Wang, F., Hu, D., et al. (2020). Deep-reaching acceleration of global mean ocean circulation over the past two decades. *Sci. Adv.* 6, eaax7727. doi: 10.1126/sciadv.aax7727
- Ivanova, D. P., McClean, J. L., Sprintall, J., and Chen, R. (2021). The oceanic barrier layer in the eastern Indian ocean as a predictor for rainfall over Indonesia and Australia. *Geophys. Res. Lett.* 48, e2021GL094519. doi: 10.1029/2021GL094519
- Jansen, M. F., Adcroft, A. J., Hallberg, R., and Held, I. M. (2015). Parameterization of eddy fluxes based on a mesoscale energy budget. *Ocean Model.* 92, 28–41. doi: 10.1016/j.ocemod.2015.05.007
- Johnson, G. C., and Lyman, J. M. (2020). Warming trends increasingly dominate global ocean. *Nat. Climate Change* 10, 757–761. doi: 10.1038/s41558-020-0822-0
- Kendall, M. G. (1948). *Rank correlation methods*.
- Klocker, A., and Abernathy, R. (2014). Global patterns of mesoscale eddy properties and diffusivities. *J. Phys. Oceanogr.* 44, 1030–1046. doi: 10.1175/JPO-D-13-0159.1
- Klocker, A., Ferrari, R., and Lacasce, J. H. (2012b). Estimating suppression of eddy mixing by mean flows. *J. Phys. Oceanogr.* 42, 1566–1576. doi: 10.1175/JPO-D-11-0205.1
- Klocker, A., Ferrari, R., Lacasce, J. H., and Merrifield, S. T. (2012). Reconciling float-based and tracer-based estimates of lateral diffusivities. *J. Mar. Res.* 70, 569–602. doi: 10.1357/002224012805262743
- Klocker, A., and Marshall, D. P. (2014). Advection of baroclinic eddies by depth mean flow. *Geophys. Res. Lett.* 41, 3517–3521. doi: 10.1002/2014GL060001
- Kozalka, I. M., and LaCasce, J. H. (2010). Lagrangian Analysis by clustering. *Ocean Dyn.* 60, 957–972. doi: 10.1007/s10236-010-0306-2
- LaCasce, J., and Bower, A. (2000). Relative dispersion in the subsurface north Atlantic. *J. Mar. Res.* 58, 863–894. doi: 10.1357/002224000763485737
- Lagerloef, G. S., Mitchum, G. T., Lukas, R. B., and Niiler, P. P. (1999). Tropical Pacific near-surface currents estimated from altimeter, wind, and drifter data. *J. Geophys. Res.: Oceans* 104, 23313–23326. doi: 10.1029/1999JC900197
- Landschützer, P., Gruber, N., and Bakker, D. C. (2016). Decadal variations and trends of the global ocean carbon sink. *Global Biogeochem. Cycles* 30, 1396–1417. doi: 10.1002/2015GB005359
- Lee, K., Nam, S., Cho, Y.-K., Jeong, K.-Y., and Byun, D.-S. (2022). Determination of long-term, (1993–2019) sea level rise trends around the Korean peninsula using ocean tide-corrected, multi-mission satellite altimetry data. *Front. Mar. Sci.* 9, 810549. doi: 10.3389/fmars.2022.810549
- Liu, R., Wang, G., Chapman, C., and Chen, C. (2022). The attenuation effect of jet filament on the eastward mesoscale eddy lifetime in the southern ocean. *J. Phys. Oceanogr.* 52, 805–822. doi: 10.1175/JPO-D-21-0030.1
- Lumpkin, R., and Elipot, S. (2010). Surface drifter pair spreading in the north Atlantic. *J. Geophys. Res.: Oceans* 115, C120117. doi: 10.1029/2010JC006338
- Ma, C., Yang, J., Wu, D., and Lin, X. (2010). The kuroshio extension: a leading mechanism for the seasonal sea-level variability along the west coast of Japan. *Ocean Dyn.* 60, 667–672. doi: 10.1007/s10236-009-0239-9
- Mann, H. B. (1945). Nonparametric tests against trend. *Econ.: J. econ. Soc.* 13, 245–259. doi: 10.2307/1907187
- Martinez-Moreno, J., Hogg, A. M., England, M. H., Constantinou, N. C., Kiss, A. E., and Morrison, A. K. (2021). Global changes in oceanic mesoscale currents over the satellite altimetry record. *Nat. Climate Change* 11, 397–403. doi: 10.1038/s41558-021-01006-9

- Mudelsee, M. (2019). Trend analysis of climate time series: a review of methods. *Earth-science Rev.* 190, 310–322. doi: 10.1016/j.earscirev.2018.12.005
- Nan, F., Yu, F., Xue, H., Wang, R., and Si, G. (2015). Ocean salinity changes in the northwest pacific subtropical gyre: the quasi-decadal oscillation and the freshening trend. *J. Geophys. Res.: Oceans* 120, 2179–2192. doi: 10.1002/2014JC010536
- Naveira Garabato, A. C., Ferrari, R., and Polzin, K. L. (2011). Eddy stirring in the southern ocean. *J. Geophys. Res.: Oceans* 116, C09019. doi: 10.1029/2010JC006818
- Ohlson, J. A., and Kim, S. (2015). Linear valuation without OLS: the theil-sen estimation approach. *Rev. Accounting Stud.* 20, 395–435. doi: 10.1007/s11142-014-9300-0
- Patara, L., Böning, C. W., and Biastoch, A. (2016). Variability and trends in southern ocean eddy activity in $1/12^\circ$; ocean model simulations. *Geophys. Res. Lett.* 43, 4517–4523. doi: 10.1002/2016GL069026
- Peng, Q., Xie, S.-P., Wang, D., Huang, R. X., Chen, G., Shu, Y., et al. (2022). Surface warming-induced global acceleration of upper ocean currents. *Sci. Adv.* 8, eabj8394. doi: 10.1126/sciadv.abj8394
- Piontkovski, S. A., Al-Tarshi, M. H., Al-Ismaili, S. M., Al-Jardani, S., and Al-Alawi, Y. (2019). Inter-annual variability of mesoscale eddy occurrence in the western Arabian Sea. *Int. J. Oceans Oceanogr.* 13, 1–23.
- Risaro, D. B., Chidichimo, M. P., and Piola, A. R. (2022). Interannual variability and trends of sea surface temperature around southern south America. *Front. Mar. Sci.* 9, 213. doi: 10.3389/fmars.2022.829144
- Roach, C. J., Balwada, D., and Speer, K. (2016). Horizontal mixing in the southern ocean from argo float trajectories. *J. Geophys. Res.: Oceans* 121, 5570–5586. doi: 10.1002/2015JC011440
- Roach, C. J., Balwada, D., and Speer, K. (2018). Global observations of horizontal mixing from argo float and surface drifter trajectories. *J. Geophys. Res.: Oceans* 123, 4560–4575. doi: 10.1029/2018JC013750
- Rypina, I. I., Kamenkovich, I., Berloff, P., and Pratt, L. J. (2012). Eddy-induced particle dispersion in the near-surface north Atlantic. *J. Phys. Oceanogr.* 42, 2206–2228. doi: 10.1175/JPO-D-11-0191.1
- Sa'adi, Z., Shahid, S., Ismail, T., Chung, E.-S., and Wang, X.-J. (2019). Trends analysis of rainfall and rainfall extremes in Sarawak, Malaysia using modified Mann-Kendall test. *Meteorol. Atmos. Phys.* 131, 263–277. doi: 10.1007/s00703-017-0564-3
- Sallee, J.-B., Speer, K., and Rintoul, S. (2011). Mean-flow and topographic control on surface eddy-mixing in the southern ocean. *J. Mar. Res.* 69, 753–777. doi: 10.1357/002224011799849408
- Schulte, J. A., Najjar, R. G., and Li, M. (2016). The influence of climate modes on streamflow in the mid-Atlantic region of the united states. *J. Hydrol.: Reg. Stud.* 5, 80–99. doi: 10.1016/j.ejrh.2015.11.003
- Sen, P. K. (1968). Estimates of the regression coefficient based on kendall's tau. *J. Am. Stat. Assoc.* 63, 1379–1389. doi: 10.1080/01621459.1968.10480934
- Stammer, D. (1998). On eddy characteristics, eddy transports, and mean flow properties. *J. Phys. Oceanogr.* 28, 727–739. doi: 10.1175/1520-0485(1998)028<0727:OECETA>2.0.CO;2
- Steinkamp, K., and Gruber, N. (2015). Decadal trends of ocean and land carbon fluxes from a regional joint ocean-atmosphere inversion. *Global Biogeochem. Cycles* 29, 2108–2126. doi: 10.1002/2014GB004907
- Sun, W., Yang, J., Tan, W., Liu, Y., Zhao, B., He, Y., et al. (2021). Eddy diffusivity and coherent mesoscale eddy analysis in the southern ocean. *Acta Oceanol. Sin.* 40, 1–16. doi: 10.1007/s13131-021-1881-4
- Syst, E., Attribution, C. C., Global, W., Level, S., Group, B., and Cazenave, A. (2018). Global sea-level budget 1993 – Present. *Earth Sys. Sci. Data* 1 (3), 1551–1590. doi: 10.5194/essd-10-1551-2018
- Taylor, G. I. (1915). I. eddy motion in the atmosphere. *Philos. Trans. R. Soc. London. Ser. A Containing Pap. Math. Phys. Character* 215, 1–26. doi: 10.1098/rsta.1915.0001
- Theil, H. (1950). A rank-invariant method of linear and polynomial regression analysis, I, II, III, nederl. *Akad. Wetensch. Proc.* 53, 386–392, 521–525, 1397–1412. doi: 10.1007/978-94-011-2546-8_20
- Tulloch, R., Marshall, J., Hill, C., and Smith, K. S. (2011). Scales, growth rates, and spectral fluxes of baroclinic instability in the ocean. *J. Phys. Oceanogr.* 41, 1057–1076. doi: 10.1175/2011JPO4404.1
- Wei, H., and Wang, Y. (2021). Full-depth scalings for isopycnal eddy mixing across continental slopes under upwelling-favorable winds. *J. Adv. Model. Earth Syst.* 13, e2021MS002498. doi: 10.1029/2021MS002498
- Xu, L., Ding, Y., and Xie, S.-P. (2021). Buoyancy and wind driven changes in subantarctic mode water during 2004–2019. *Geophys. Res. Lett.* 48, e2021GL092511. doi: 10.1029/2021GL092511
- Yamaguchi, R., and Suga, T. (2019). Trend and variability in global upper-ocean stratification since the 1960s. *J. Geophys. Res.: Oceans* 124, 8933–8948. doi: 10.1029/2019JC015439
- Yang, H., Qiu, B., Chang, P., Wu, L., Wang, S., Chen, Z., et al. (2018). Decadal variability of eddy characteristics and energetics in the kuroshio extension: unstable versus stable states. *J. Geophys. Res.: Oceans* 123, 6653–6669. doi: 10.1029/2018JC014081
- Yu, X., Ponte, A. L., Elipot, S., Menemenlis, D., and Abernathey, R. (2019). Surface kinetic energy distributions in the global oceans from a high-resolution numerical model and surface drifter observations. *Geophys. Res. Lett.* 46 (16), 9757–9766. doi: 10.1029/2019GL083074
- Yue, S., and Wang, C. (2004). The Mann-Kendall test modified by effective sample size to detect trend in serially correlated hydrological series. *Water Resour. Manage.* 18, 201–218. doi: 10.1023/B:WARM.0000043140.61082.60
- Zhao, B., Lin, P., Hu, A., Liu, H., Ding, M., Yu, Z., et al. (2022). Uncertainty in Atlantic multidecadal oscillation derived from different observed datasets and their possible causes. *Front. Mar. Sci.* 9, 2148. doi: 10.3389/fmars.2022.1007646
- Zhurbas, V., and Oh, S. I. (2004). Drifter-derived maps of lateral diffusivity in the pacific and Atlantic oceans in relation to surface circulation patterns. *J. Geophys. Res.* 109, C05015. doi: 10.1029/2003JC002241